Journal of Power Sources 195 (2010) 3870–3881

Contents lists available at ScienceDirect

Journal of Power Sources

journal homepage: www.elsevier.com/locate/jpowsour

Lattice Boltzmann simulations of water transport in gas diffusion layer of a polymer electrolyte membrane fuel cell

Liang Hao, Ping Cheng*

Ministry of Education Key Laboratory of Power Machinery and Engineering, School of Mechanical Engineering, Shanghai Jiaotong University, DongChuan Road 800#, Shanghai 200240, PR China

ARTICLE INFO

Article history:
Received 28 September 2009
Received in revised form
23 November 2009
Accepted 25 November 2009
Available online 1 December 2009

Keywords:
Lattice Boltzmann method
Water transport
Gas diffusion layer
Wettability
Saturation

ABSTRACT

The effect of wettability on water transport dynamics in gas diffusion layer (GDL) is investigated by simulating water invasion in an initially gas-filled GDL using the multiphase free-energy lattice Boltzmann method (LBM). The results show that wettability plays a significant role on water saturation distribution in two-phase flow in the uniform wetting GDL. For highly hydrophobicity, the water transport falls in the regime of capillary fingering, while for neutral wettability, water transport exhibits the characteristic of stable displacement, although both processes are capillary force dominated flow with same capillary numbers. In addition, the introduction of hydrophilic paths in the GDL leads the water to flow through the hydrophilic pores preferentially. The resulting water saturation distributions show that the saturation in the GDL has little change after water breaks through the GDL, and further confirm that the selective introduction of hydrophilic passages in the GDL would facilitate the removal of liquid water more effectively, thus alleviating the flooding in catalyst layer (CL) and GDL. The LBM approach presented in this study provides an effective tool to investigate water transport phenomenon in the GDL at pore-scale level with wettability distribution taken into consideration.

1. Introduction

The advantages of high energy efficiency and low pollution of environment have made the polymer electrolyte membrane fuel cells (PEMFCs) an attractive alternative power source for automotive and portable applications. In a PEMFC, hydrogen and oxygen are supplied as the reactants and water is produced in the catalyst layer (CL) of the cathode owing to electrochemical reactions there. Water management is regarded as a critical issue on the performance of PEMFCs [1]. On the one hand, the membrane should have sufficient hydration to maintain good proton conductivity. On the other hand, too much water generated and accumulated in the cathode can cause flooding in CL, resulting in the mass transport limitations with water blocking the transport of reaction gases to the active reaction sites, thus severely lowering the performance of PEMFCs [2]. The gas diffusion layer (GDL), which is placed between the gas channel and CL, therefore, plays an important role on the removal of unwanted water from the CL.

Recently, much attention has been given to the investigation of water flow in GDL by many researchers using both numerical simulations and experiments. The unsaturated flow [3] and multiphase mixture approaches [4,5] were two widely used macroscopic models for two-phase transport in GDL. In these models, the GDL was assumed as a homogeneous porous medium based on the volumetric averaging theory, and various macroscopic conservation equations were applied to describe the two-phase flow behaviors in an elementary volume. However, empirical relationships of capillary pressure–saturation and relative permeability–saturation relations must be given in the macroscopic equations for simulation of two-phase flow in the porous GDL. Due to the questionable accuracy of these empirical relations when applied to GDL materials, the macroscopic models predicted large differences in the distribution of water saturation in GDL [6]. Furthermore, the homogeneous assumption of water transport in GDL used in the macroscopic models was not supported by experimental studies [7–13]. Employing transparent fuel cells, Yang et al. [7] and Zhang et al. [8] observed that water emerged from the GDL in the form of individual droplets at specific locations of GDL surface. Litster et al. [9] used a novel method of employing fluorescence microscopy to visualize water flow within the GDL structure. Based on their observation, they suggested that the transport of water in GDL was not a converging capillary tree as proposed by Nam and Kaviany [3], but it was dominated by fingering and channeling. More advanced radiography techniques have also been employed to explore water transport in fuel cells. Using X-ray micro-tomography, Sinha et al. [10] investigated water distribution in the GDL during the purge process and showed that water distribution in the GDL was in the form of non-uniform and irregular clusters. Using the neutron

* Corresponding author. Tel.: +86 21 34206337; fax: +86 21 34206337.
E-mail address: pingcheng@sjtu.edu.cn (P. Cheng).

0378-7753/$ – see front matter © 2009 Elsevier B.V. All rights reserved.
doi:10.1016/j.jpowsour.2009.11.125

imaging technique, Pekula et al. [11] investigated water distribution and evolution in the gas flow channel and GDL of an operating PEMFC. They obtained the planar averaged water content in their fuel cell and found that water was accumulated at specific locations of the GDL along or under the channel walls. Most recently, Hickner et al. [12] and Hartnig et al. [13] used high resolution neutron radiography and X-ray radiography respectively to image an operating PEMFC and obtained a complex water content distribution in the cross-section of the cell, which was much different from the prediction by macroscopic models. Even though these visualization studies were successfully used to observe water distribution in PEMFCs and thus providing useful information on understanding water transport in GD, all of experimental methods mentioned above have their limitations when applied to investigate water transport in PEMFCs, especially in GDL. For example, the optical method by employing microscopy [7–9] is unable to penetrate the whole thickness of GDL, thus is difficult to probe water flowing within such materials. Moreover, the less water sensitivity of X-ray imaging [10,13] and low spatial resolution of neutrons imaging [11,12] also limit their use to study water transport in GDL.

Because of the shortcomings of macroscopic models and existing experimental methods, pore-scale simulations which can provide a microscopic insight of water transport within the GDL, have been performed and become a necessary complement to limited experimental studies. Using the pore network model, Sinha and Wang [14,15] studied the dynamics of liquid water transport and evolution of saturation profile in a network GDL. The effects of constant and mixed wettability distribution of GDL pores on water transport were investigated. Furthermore, Lee et al. [16,17] performed similar network simulations of capillary-driven process of water transport in the hydrophobic GDL. Although the pore network model provided more fundamental understanding of water transport and distribution in GDL than macroscopic models, it cannot describe water transport in an actual GDL microstructure. In network models, the complex morphology of real porous medium is idealized by regular spherical or cubic pores and their connection of columnar throats with assumed size distributions according to probability functions. In order to overcome this defect of network model, Schulz et al. [18] developed a full morphology model to study water invasion process in GDL based on a numerically reconstructed three-dimensional fibrous microstructure of carbon paper GDL. The capillary pressure–saturation relation and water distribution in the GDL at various capillary pressures were obtained. However, the full morphology model can only treat stationary phase distributions at a given capillary pressure, but cannot provide a detailed simulation of water transport dynamics [19].

The lattice Boltzmann method (LBM), which is a promising tool to simulate multiphase flow in porous media, can give more realistic pore-scale dynamic simulations of water transport in GDL with accurate pore geometry taken into consideration. The mesoscale kinetic base of LBM makes it very effective to deal with complex boundary condition [20] and multiphase and multicomponent flow problems [21–23]. For example, Pan et al. [24] simulated two-phase flow in a reconstructed packed-sphere bed using the LBM approach. Good agreement was achieved between the measured capillary pressure–saturation relations and the LBM simulations. In addition, some works on the application of LBM to study the transport phenomena in GDL of PEMFCs have also been carried out [25–29]. Park et al. [25] simulated gas flow through a fiber tow in the carbon cloth GDL by using single-phase LBM in solving Stokes and Brinkman equations in the void and porous tow, respectively. Hao and Cheng [26] performed a pore-scale LBM simulation of single-phase flow in a reconstructed 3D carbon paper GDL, and the anisotropic permeabilities thus obtained were found in good agreement with experimental data. Park and Li [27] presented a 2D two-phase LBM simulation of water droplet flowing through the porous structure of carbon paper GDL. Niu et al. [28] applied the LBM model to investigate the relative permeability by simulating two-phase flow in the carbon paper GDL. Sinha et al. [29] simulated liquid water drainage process and water distribution in a reconstructed non-woven GDL microstructure using two-phase LBM model. However, the application of LBM to study water dynamic invasion in the GDL with wettability distribution taken into consideration has not yet been performed in the literature.

In this paper, a pore-scale simulation of water transport dynamic behavior in a carbon paper GDL with detailed microstructure and wettability distribution is investigated using the multiphase LBM approach based on the free-energy theory [22]. The uniform velocity boundary condition was imposed at the inlet, which was suggested as a proper boundary condition for liquid water entering GDL [16]. The evolution of water distribution in the GDL pores and the cross sectional averaged water saturation profiles along the thickness of the GDL are obtained from the simulation results, and effects of wettability distribution on water transport in the GDL are discussed.

2. Theory and model description

2.1. Two-phase transport in GDL

The physics of two immiscible fluids flow in porous media has been well investigated by experiments and model studies in water resource and oil recovery research field [30–32]. According to the phase diagram proposed by Lenormand [30] and widely cited in recent pore network studies [14–17], water transport in GDL under the PEMFCs operation condition falls in the capillary fingering regime. In this regime, the water flow is strongly dominated by the capillary force while the buoyancy, viscous and inertial forces are negligible. For example, in a typical water transport process in GDL, the Bond number $Bo = g(\rho_w - \rho_a)d_p^2/\sigma$ (with g being the gravitational acceleration, $\rho_w - \rho_a$ being the density difference of water and air and d_p being the characteristic pore diameter) which denotes the ratio of gravitational and interfacial forces is of the order of 10^{-5}. At the same time, the capillary number $Ca = u_w\eta_w/\sigma$ (with u_w and η_w being the water flow velocity and water viscosity, respectively) which denotes the ratio of viscous force to surface tension force is of the order of 10^{-8}, and the Reynolds number $Re = u_w d_p/\upsilon$ (with υ being the water kinematic viscosity) which denotes the ratio of inertial force to viscous force is of the order of 10^{-5}. The values of these dimensionless numbers indicate that surface tension is much more predominant than gravitational, inertial and viscous force. Therefore, it can be concluded that the fluid density and viscosity ratios, which affect gravitational, inertial and viscous forces, respectively, have insignificant influence on the two-phase transport in GDL under such small values of Bond, capillary and Reynolds numbers.

2.2. Reconstruction of carbon paper GDL

The carbon paper or carbon cloth is generally used as the GDL in PEMFCs. These materials have microscopically complex structure with random distribution of pores sizes ranging from a few microns to tens of microns. In order to perform a pore-scale simulation of water transport in the GDL, detailed pore morphology of the GDL should first be obtained. In the present study, the method proposed by Schladitz et al. [33] based on the stochastic generation method is adopted to reconstruct the carbon paper GDL. This method was also used previously by Hao and Cheng [26] in simulating single-phase flow though carbon paper GDL and by Schulz et al. [18] in their full morphology simulation of water drainage through an initially gas-saturated GDL.

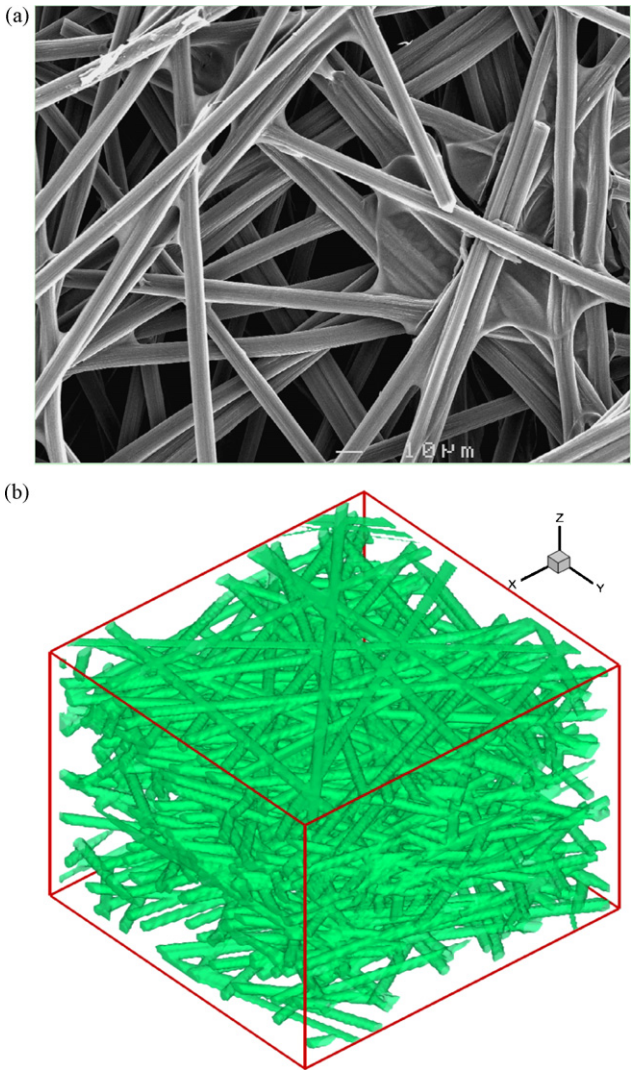

Fig. 1. Micrographs of the carbon paper GDL. (a) SEM image of the Toray 060 GDL. (b) 3D geometer of the reconstructed carbon paper microstructure.

Fig. 1(a) presents the SEM image of the Toray 060 carbon paper with randomly arranged carbon fibers in a plane. In order to simplify the numerical reconstruction of the complex real GDL, the following assumptions are made: (i) carbon fibers in GDL are cylinders with a uniform diameter; (ii) fibers are straight with infinite length and allowed to be overlapped; (iii) fibers are stochastic arranged in the material plane while their orientation to the GDL thickness direction is neglected. Based on these assumptions, the reconstruction of carbon paper is achieved by placing the fibers on one plane with arbitrary positions and orientations layer by layer with the prescribed GDL size, porosity and fiber diameter. Fig. 1(b) shows the microstructure of the reconstructed carbon paper GDL with the size of $150 \times 150 \times 127$ lattice grid and a given porosity of 0.79 and fiber diameters of 7.5 μm, which are chosen according to the actual Toray carbon paper GDL [9].

2.3. LBM model

Several lattice Boltzmann methods have been developed for simulating multiphase flow problems, in which the intermolecular potential model proposed by Shan and Chen [21] and free-energy model proposed by Swift et al. [22] are two most widely used approaches. In the intermolecular potential model, the nearest-neighboring interaction between fluid particles is introduced to describe the intermolecular potential, and the two immiscible fluids achieve separation if the interaction force between the fluids is larger than a threshold value. However, as pointed out in [34], the surface tension in this model is actually a numerical artifact. In contrast, the free-energy model has a firm theoretical basis. The surface tension as well as the contact angle when solid is present can be directly derived from the free-energy function based on Cahn-Hilliard theory [22]. Therefore, the free-energy LBM is adopted for numerical simulation in the present work.

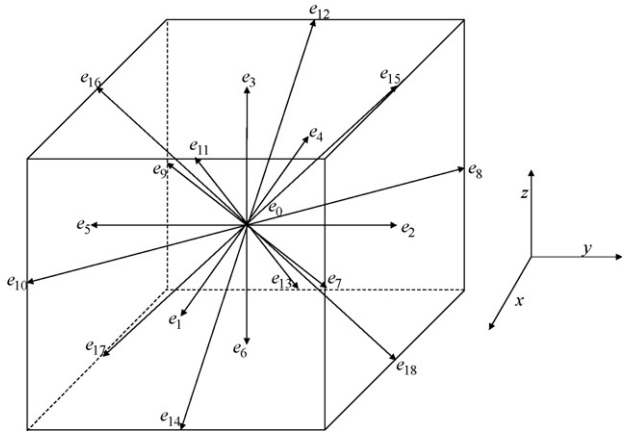

Fig. 2. Lattice velocity directions of the three-dimension 19-velocity (D3Q19) model.

In the free-energy LBM model, the binary fluids flow is described by the evolution of distribution functions $f_\alpha(x, t)$ and $g_\alpha(x, t)$ as the following equations:

$$f_\alpha(\boldsymbol{r} + e_\alpha \delta t, t + \delta t) - f_\alpha(\boldsymbol{r}, t) = -\frac{f_\alpha(\boldsymbol{r}, t) - f_\alpha^{eq}(\boldsymbol{r}, t)}{\tau_f} + F_\alpha \tag{1a}$$

$$g_\alpha(\boldsymbol{r} + e_\alpha \delta t, t + \delta t) - g_\alpha(\boldsymbol{r}, t) = -\frac{g_\alpha(\boldsymbol{r}, t) - g_\alpha^{eq}(\boldsymbol{r}, t)}{\tau_g} \tag{1b}$$

where τ_f and τ_g are two independent relaxation parameters, which are related to the fluid viscosity and phase interface mobility M as follows:

$$\nu = \frac{(\tau_f - 0.5)\delta t}{3}; \quad M = \Gamma(\tau_g - 0.5)\delta t \tag{2}$$

where Γ is the coefficient controlling the phase interface diffusion. f_α^{eq} and g_α^{eq} in Eq. (1) are the equilibrium distributions of f_α and g_α, which are given as the function of local density ρ, velocity u and phase parameter φ, respectively:

$$f_\alpha^{eq} = A_\alpha + w_\alpha \rho \left[3\frac{\boldsymbol{e}_\alpha \cdot \boldsymbol{u}}{c^2} + 4.5\frac{(\boldsymbol{e}_\alpha \cdot \boldsymbol{u})^2}{c^4} - 1.5\frac{\boldsymbol{u} \cdot \boldsymbol{u}}{c^2} \right] \tag{3a}$$

$$g_\alpha^{eq} = H_\alpha + w_\alpha \phi \left[3\frac{\boldsymbol{e}_\alpha \cdot \boldsymbol{u}}{c^2} + 4.5\frac{(\boldsymbol{e}_\alpha \cdot \boldsymbol{u})^2}{c^4} - 1.5\frac{\boldsymbol{u} \cdot \boldsymbol{u}}{c^2} \right] \tag{3b}$$

with A_α and H_α being the coefficients whose values can be found in our previous work [35], and $c = \delta x/\delta t$ being the lattice speed. For the three-dimension 19-velocity (D3Q19) model as shown in Fig. 2, the lattice velocity vector e_α and the weight coefficients w_α are given as follows:

$$e_\alpha = \begin{cases} (0,0,0), & \alpha = 0; \\ (\pm 1,0,0)c,\ (0,\pm 1,0)c,\ (0,0\pm 1)c, & \alpha = 1-6; \\ (\pm 1,\pm 1,0)c,\ (\pm 1,0,\pm 1)c,\ (0,\pm 1,\pm 1)c, & \alpha = 7-18. \end{cases}$$
$$w_\alpha = \begin{cases} 1/3, & \alpha = 0; \\ 1/18, & \alpha = 1-6; \\ 1/36, & \alpha = 7-18. \end{cases} \tag{4}$$

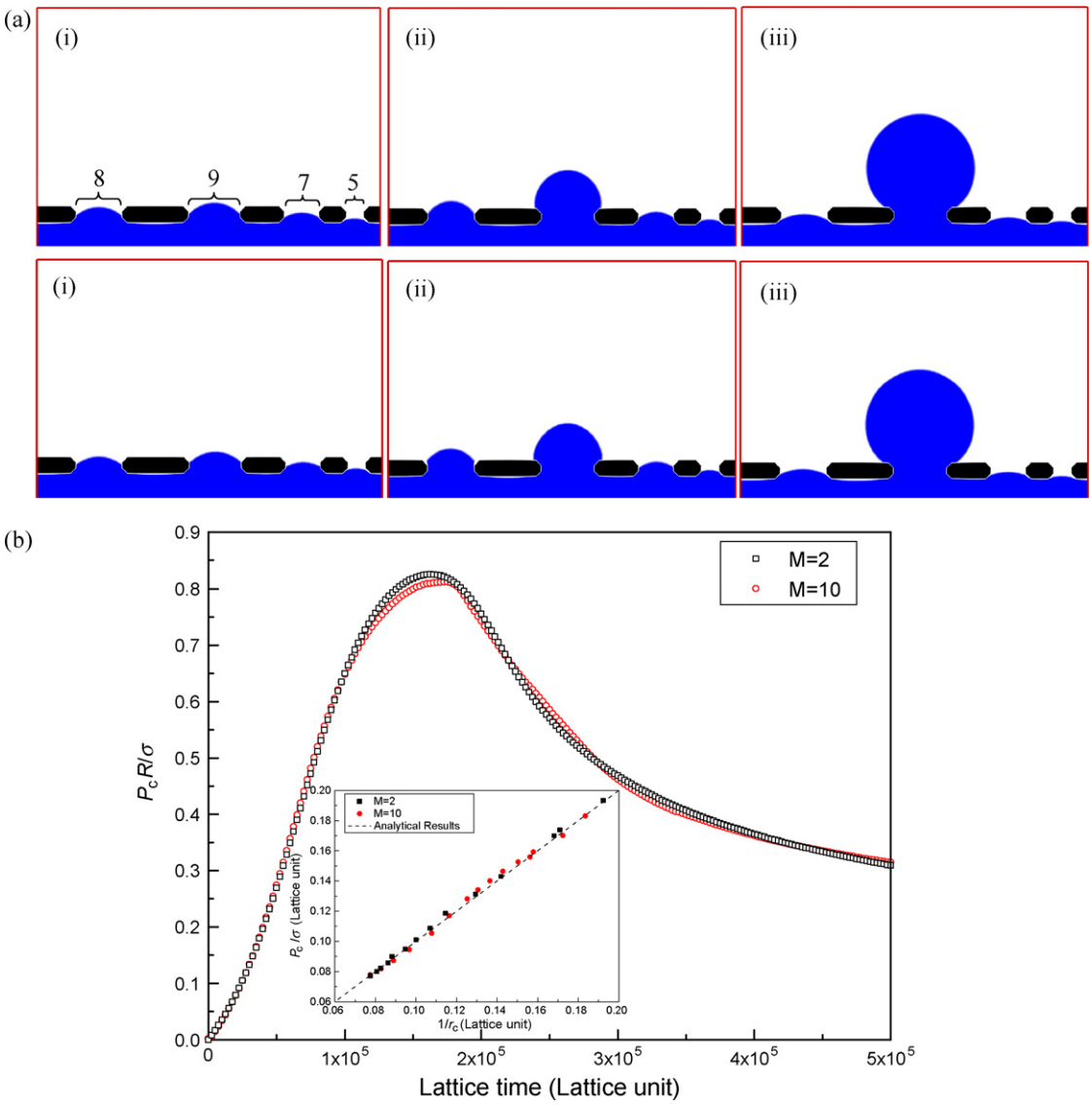

Fig. 3. (a) Invasion of non-wetting phase through a perforated plate with different size pores for two different viscosity ratios $M = 2$ (top) and $M = 10$ (bottom) (blue area denotes the non-wetting phase). (i) $t = 1.1 \times 10^5$ lattice time, (ii) $t = 2.0 \times 10^5$ lattice time, (iii) $t = 3.1 \times 10^5$ lattice time. (b) Capillary pressure variation with time during the non-wetting phase invasion for two different viscosity ratios $M = 2$ and $M = 10$. (Insert shows the comparison of the LBM simulates with the analytical results for P_c/σ as a function of the breakthrough droplet curvature radius.) (For interpretation of the references to color in this figure legend, the reader is referred to the web version of the article.)

The last term F_α in Eq. (1a) represents the body force components in the lattice space, which is given by [20]

$$F_\alpha = 3w_\alpha \frac{\boldsymbol{e}_\alpha \cdot \boldsymbol{F}}{c^2} \tag{5}$$

with **F** being the body force. The macroscopic local density ρ, momentum ρu and phase parameter φ are obtained from the distribution functions $f_\alpha(x, t)$ and $g_\alpha(x, t)$ by

$$\rho = \sum_{\alpha=0}^{18} f_\alpha; \qquad \rho\mathbf{u} = \sum_{\alpha=0}^{18} f_\alpha \mathbf{e}_\alpha + \frac{\delta t}{2}\mathbf{F}; \qquad \varphi = \sum_{\alpha=0}^{18} g_\alpha \tag{6}$$

The surface tension between different phases and the contact angle when solid boundary is presented can be derived from the free-energy function F. For the Landau free-energy function

$$F = \int_v dV \left(\psi(\varphi) + \frac{\kappa}{2}(\nabla\varphi)^2\right) + \int_S dS\, \psi(\varphi_s) \tag{7}$$

the bulk free-energy density $\psi(\varphi)$ can be chosen in the form of a double-well potential

$$\psi(\varphi) = -\frac{A}{2}\varphi^2 + \frac{B}{4}\varphi^4 \tag{8}$$

where A and B are two parameters, which are chosen by positive values for phase separation in present study. The chemical potential μ is derived from the free-energy density function by

$$\mu = \frac{\partial\psi}{\partial\varphi} - \kappa\nabla^2\varphi = -A\varphi + B\varphi^3 - \kappa\nabla^2\varphi \tag{9}$$

The minimization of the chemical potential in bulk results in

$$\mu = -A\varphi + B\varphi^3 - k\nabla^2\varphi = 0 \tag{10}$$

Thus, the equilibrium phase parameter φ_0 in the bulk of the two different fluids follows $\varphi_0 = \pm(A/B)^{1/2} = \pm 1$ when restricting the value $A = B$. The surface tension can be determined from the interface width ξ and the equilibrium phase parameter in the bulk phase

φ_0 as [36]

$$\sigma = \frac{4\kappa}{3\xi}\varphi_0^2 \tag{11}$$

Employing the Chapman–Enskog multiscale analysis for D3Q19 model, the distribution evolution functions Eqs. (1a) and (1b) can lead to the Navier–Stokes equations for two-phase system and a phase parameter evolution equation in the incompressible limit [22]:

$$\frac{\partial \rho}{\partial t} + \nabla \cdot (\rho \boldsymbol{u}) = 0, \tag{12a}$$

$$\frac{\partial (\rho \boldsymbol{u})}{\partial t} + \nabla \cdot (\rho \boldsymbol{u}\boldsymbol{u}) = -\nabla \cdot \boldsymbol{P} + \nabla \cdot (\rho \nu \nabla \boldsymbol{u}) + \boldsymbol{F} \tag{12b}$$

$$\frac{\partial \varphi}{\partial t} + \nabla \cdot (\varphi \mathbf{u}) = M\nabla^2 \mu, \tag{12c}$$

where **P** is the complete thermodynamic pressure tensor and is given by [36]

$$P = p\boldsymbol{I} + \kappa(\nabla\varphi)(\nabla\varphi)^T \tag{13}$$

with **I** being the second-order unit tensor and p being the scale part of the pressure tensor which can be expressed by [36]

$$p = \frac{c^2}{3}\rho - \frac{A}{2}\varphi^2 + \frac{3B}{4}\varphi^4 - \kappa\varphi\nabla^2\varphi - \frac{\kappa}{2}(\nabla\varphi)^2 \tag{14}$$

In the binary liquid system with unequal viscosities, the viscosity at the phase interface can be evaluated by

$$\nu = \frac{\varphi + \varphi_0}{2\varphi_0}(\nu_1 - \nu_2) + \nu_2 \tag{15}$$

where ν_1 and ν_2 denote the viscosities of the two different fluids.

Furthermore, the surface energy between the solid wall and fluid is described by the second term on the right hand side in Eq. (7) with φ_s being the phase parameter of the wall. Following the analysis in [37], the contact angle is related to the wetting potential Θ by

$$\cos(\theta) = \frac{(1+\Theta)^{1.5} - (1-\Theta)^{1.5}}{2} \tag{16}$$

where the wetting potential Θ is given by

$$\Theta = -\frac{\partial\varphi}{\partial\vec{n}}\sqrt{\frac{2k}{A}} \tag{17}$$

with $\partial\varphi/\partial\vec{n}$ being phase parameter derivative at the wall.

More detailed description of the free-energy LBM and the boundary conditions implementation can be found in our previous work on numerical simulation of droplet dynamics on a hydrophobic micro-channel [35].

3. Model validation

Two numerical experiments were performed to validate the present multiphase LBM model:

3.1. Non-wetting phase invasion through a perforated plate

Fig. 3(a) shows the invasion of the non-wetting phase through a perforated plate (with four different size pores of 9 lattice length, 8 lattice length, 7 lattice length and 5 lattice, respectively) for two different viscosity ratios of $M = 2$ and $M = 10$, where M is defined as the ratio of now-wetting phase viscosity to wetting phase viscosity. A 2D computational domain of 60×50 lattices including the perforated plate is considered here. The non-wetting phase fluid, which has a contact angle of $\theta = 145^\circ$ with the plate wall, was initially placed under the plate. The gravitational force was ignored and the uniform velocity boundary condition was imposed at the bottom boundary of the computational domain with the resulting capillary number of the order of 10^{-6}. From the results of LBM simulation shown in Fig. 3(a), it can be seen that the invasion processes for different viscosity ratios are almost the same and the non-wetting phase only invades the largest pore of the plate, indicating that the two-phase flow is dominated by capillary force where viscous effects is negligible. Comparing the evolution pictures in this figure, it is found that the phase interfaces in smaller pores recede after non-wetting phase breaks through the largest pore at $t = 3.1 \times 10^5$ lattice time. According to the Laplace's law, the pressure difference of the phase interface, which is defined as the capillary pressure P_c, is related to the interface curvature radius r_c by

$$P_c = c\frac{\sigma}{r_c} \quad (\text{with } c = 1 \text{ for 2D}, \ \ c = 2 \ \text{ for } \ 3\text{D}) \tag{18}$$

When the non-wetting phase contacting with the pores in the plate, the capillary resistance force resists the invasion of the non-wetting phase. Due to the constant inlet flux, the capillary pressure increases against the capillary resistance, resulting in the decrease of phase interface curvature radius from Eq. (18) and the advance of phase interface into the pores. However, after non-wetting phase breaks through the largest pore, which has the smallest capillary resistance, the capillary pressure suddenly drops as shown in Fig. 3(b). As a result, the phase interface curvature radius r_c should increase to fit the decrease of the capillary pressure based on Eq. (18), thus the phase interfaces in smaller pores recede. It should be noted that the capillary pressure in Fig. 3(b) is expressed as a dimensionless form P_cR/σ with R being the largest pore radius.

Moreover, the capillary pressure for the non-wetting phase breaks through the largest pore can be obtained from the Young–Laplace equation by substituting curvature radius $r_c = R/\cos(\pi - \theta)$ in Eq. (18) to give

$$P_c = -c\frac{\sigma\cos\theta}{R} \quad (\text{with } \ c = 1 \text{ for 2D}, \ \ c = 2 \ \text{ for 3D}) \tag{19}$$

From Eq. (19), the analytical dimensionless breakthrough capillary pressure P_cR/σ is 0.819, which is good agreement with the value of 0.825 for $M = 2$ and 0.812 for $M = 10$ from LBM simulations. The relation between P_c/σ with the variation of curvature radius r_c of the breakthrough droplet is plotted in the insert of Fig. 3(b). Again, the LBM simulated results for two viscosity ratios ($M = 2$, 10) are in excellent agreement with analytical results from Eq. (18), indicating that the two-phase flow can be regarded as quasi-

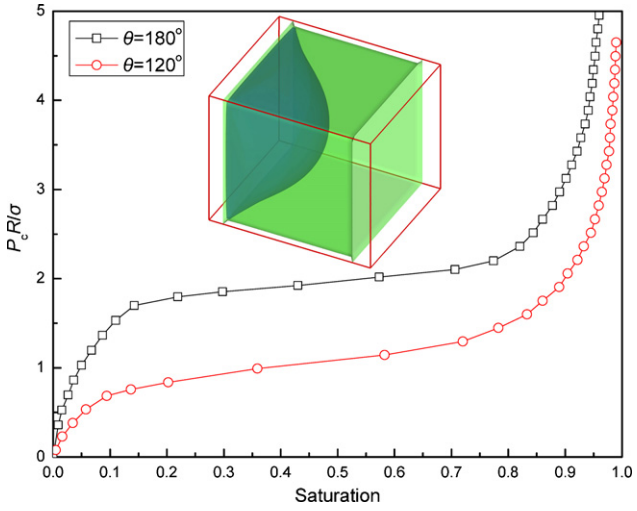

Fig. 4. The capillary pressure curves by non-wetting phase displacement in a square capillary channel with respect to different contact angle θ. (Insert shows the shape of the non-wetting phase entering the capillary channel.)

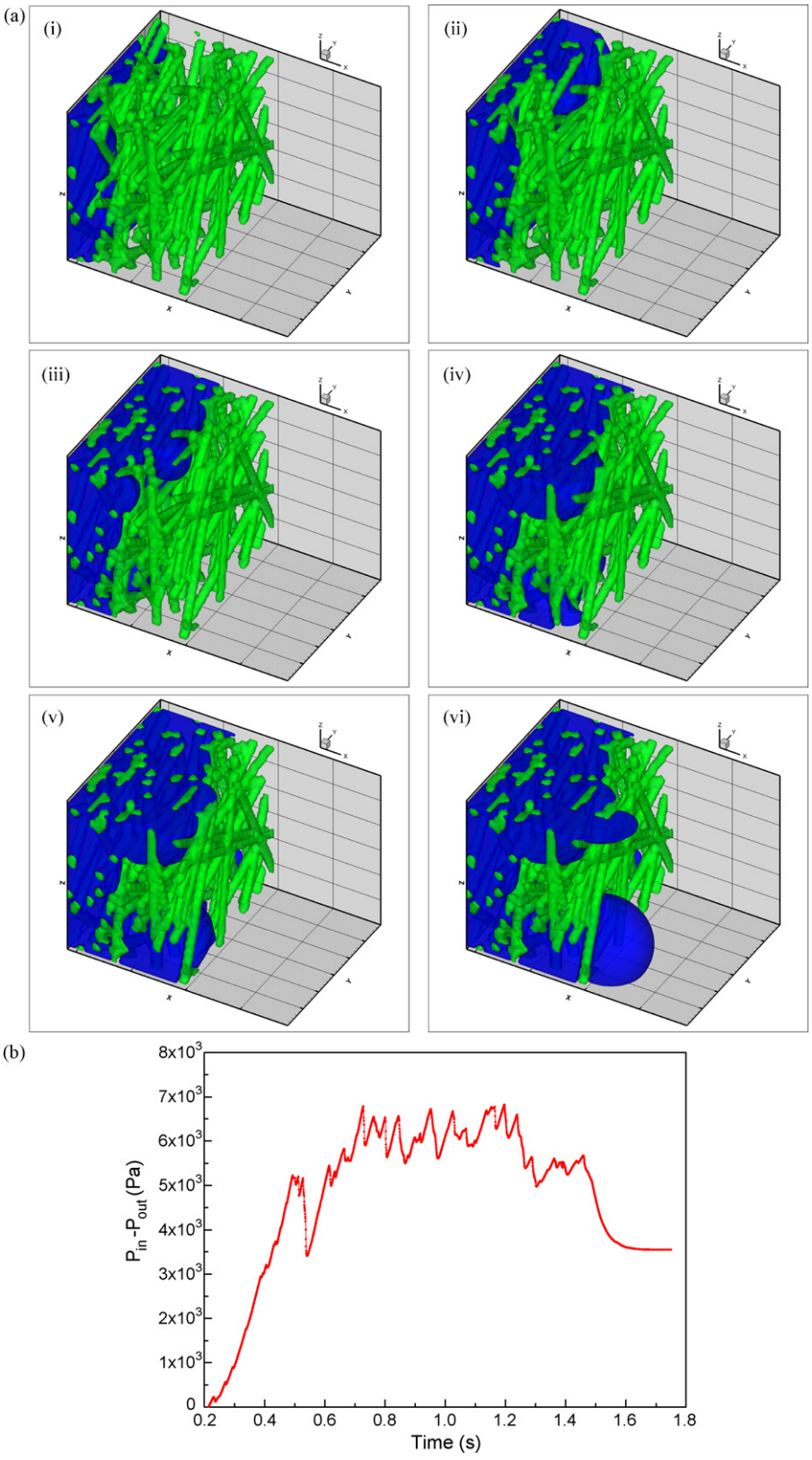

Fig. 5. (a) Snapshots of the water behavior in the reconstructed GDL microstructure with fiber contact angle of 115° and capillary number of 4.5×10^{-7} (blue area denotes the water). (i) $t = 0.85$ s, (ii) $t = 1.05$ s, (iii) $t = 1.25$ s, (iv) $t = 1.35$ s, (v) $t = 1.45$ s, (vi) $t = 1.50$ s. (b) Capillary pressure variation with time during the water invasion in the reconstructed GDL with fiber contact angle of 115° and capillary number of 4.5×10^{-7}. (c) Cross-section images of water distribution in the reconstructed GDL with fiber contact angle of 115° and capillary number of 4.5×10^{-7} (blue area denotes the water). (i) $t = 0.85$ s, (ii) $t = 1.05$ s, (iii) $t = 1.35$ s, (iv) $t = 1.50$ s. (d) Evolution of the water saturation profiles along the through-plane direction of the GDL with fiber contact angle of 115° and capillary number of 4.5×10^{-7}. (For interpretation of the references to color in this figure legend, the reader is referred to the web version of the article.)

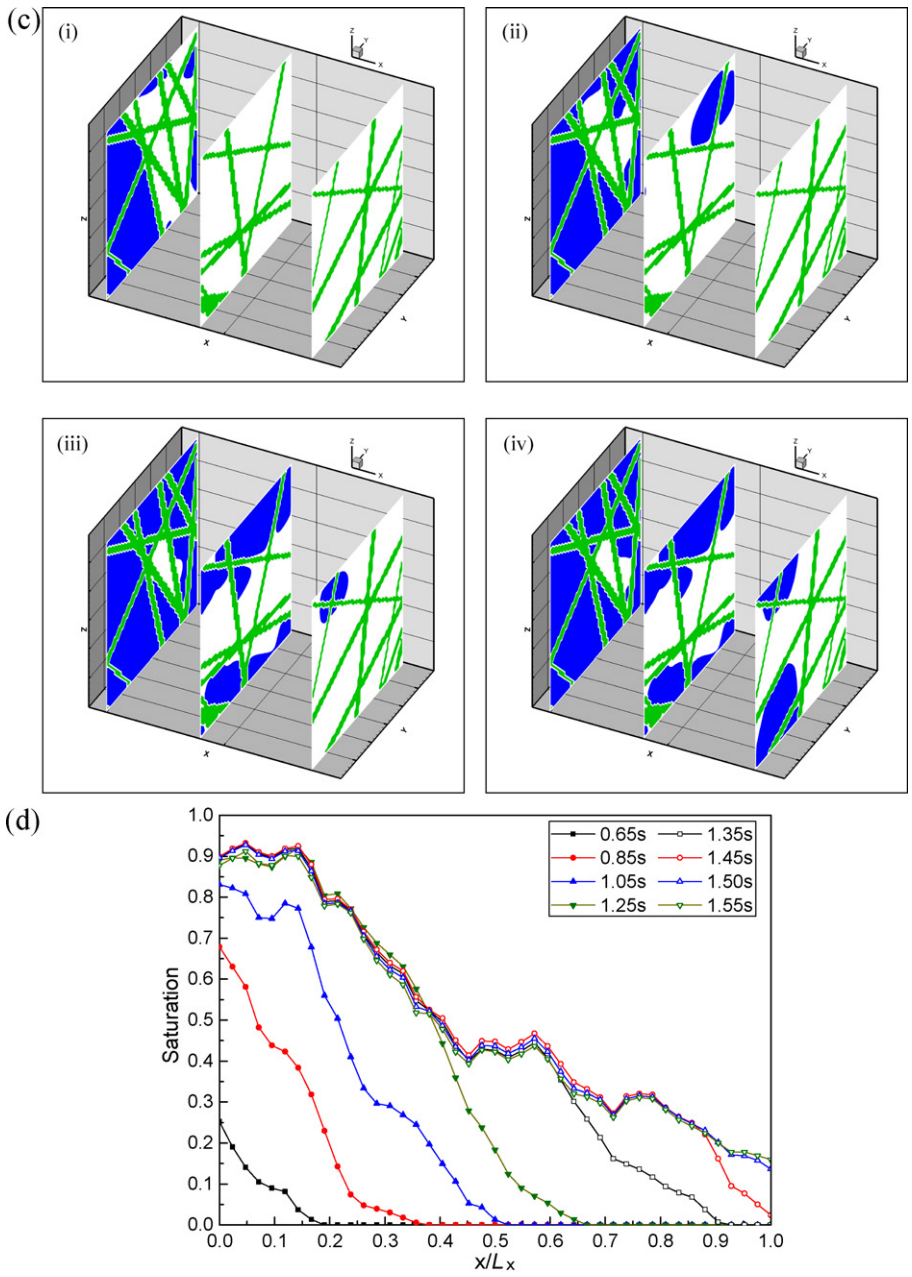

Fig. 5. (*Continued*).

equilibrium process during the non-wetting phase invasion which is dominated by the capillary force.

3.2. Two-phase displacement in a capillary channel

Next, two-phase displacement was performed by simulating the non-wetting phase drainage the wetting phase in a 3D capillary channel (with a square cross-section of 50×50 lattices and a length of 60 lattices). A non-wetting phase and a wetting phase reservoirs with 5 lattices size were added to the front end and back end of the channel, respectively. Pressure boundary conditions were imposed at the two reservoirs and the drainage process was simulated by decreasing the wetting phase reservoir pressure while keeping the pressure in the non-wetting phase reservoir unchanged as was done in [24]. The difference between the non-wetting phase pressure and wetting phase pressure, that is the capillary pressure, increases gradually and drives the non-wetting phase into the channel which is initially filled by wetting phase.

Fig. 4 shows the LBM simulated capillary pressure versus the non-wetting phase saturation for the capillary channel with different contact angles. The capillary pressure is also expressed in the dimensionless form of $P_c R/\sigma$ with R being the capillary tube equivalent radius. The analytical entry capillary pressure, that is the minimum capillary pressure for the non-wetting phase driven into the channel, can be obtained from Eq. (19) with $c = 2$, which is equal to 2.0 for $\theta = 180^\circ$ and equal to 1.0 for $\theta = 120^\circ$. These values agree well with simulation values shown in Fig. 4. The shape of the non-wetting phase entering the square capillary channel with $\theta = 180^\circ$ is also shown in the insert of Fig. 4. It clearly shows that the corners of the channel are occupied by the wetting phase during the drainage process.

4. Results and discussion

We now return to the problem of water transport through a reconstructed 3D GDL microstructure. In order to keep a reasonable

computational cost, a reconstructed GDL with its cross-section (in *yz*-plane) of 60 × 60 lattice nodes and thickness (in *x*-direction) of 45 lattice nodes (with one lattice distance representing 2.5 μm of the physical length) was chosen in present study. The grid size effect was tested by performing non-wetting phase drainage simulations in this reconstructed GDL with three different lattice resolutions of 3.8 μm, 2.5 μm and 1.5 μm, respectively. The results showed almost the same capillary pressure curves for the lattice resolutions of 2.5 μm and 1.5 μm. Thus, a lattice distance with 2.5 μm was adopted in this study.

In the following simulation studies, the uniform velocity boundary condition was specified at the inlet and the constant pressure boundary condition was specified at the outlet. In order to reduce the influence of the GDL fiber on the inlet boundary, 5 layer lattices were added between the GDL and the inlet boundary. Moreover, a void space including 35 layer lattices was also added between the GDL and the outlet boundary to simulate water droplet formation through the GDL. Thus, the total computational domain has the size of 60 × 60 × 85 lattice nodes in present study. To relate the lattice units to the physical units, the dimension analogy was performed in both lattice space and physical space. For the kinematic viscosity ν and pressure P, they satisfy

$$\frac{\upsilon_L}{\delta x_L^2/\delta t_L} = \frac{\upsilon_p}{\Delta x_p^2/\Delta t_p}; \qquad \frac{P_L \delta x_L}{\sigma_L} = \frac{P_p \Delta x_p}{\sigma_p} \tag{20}$$

where subscripts L and p denote the quantities in lattice space and physical space, respectively, and the physical length Δx_p is 2.5 μm. The lattice length δx_L and lattice time step δt_L in present LBM both are unity. As a result, the physical time step and physical pressure can be obtained from Eq. (20) by

$$\Delta t_p = \frac{\upsilon_L}{\upsilon_p}\Delta x_p^2; \qquad P_p = \frac{P_L \sigma_p}{\Delta x_p \sigma_L} \tag{21}$$

Based on the discussion in Section 2.1 that the gravitational, inertial and viscosity forces are negligible comparing with the capillary force for water transport in GDL, the effects of density and viscosity ratios on two-phase transport in GDL can be safely neglected in present study. For this reason, we arbitrarily set the density of water and gas to be same and viscosity ratio of water and gas to be 2.0 to avoid the numerical instability which may occur for large density and viscosity ratios in present LBM. It should be noted that the arbitrarily assumed values of density and viscosity ratios in porous media problems was also adopted in previous two-phase LBM simulations using intermolecular potential model [24,27,29]. Based on the physical parameters of surface tension and water kinematic viscosity of 0.0645 N m^{-1} and 4.13 × 10^{-7} m^2 s^{-1} at 70 °C [17], we obtained the physical time step $\Delta t_p = 5 \times 10^{-6}$ s, if the water kinematic viscosity of 1/3 is used in the lattice space. The uniform velocity at the inlet boundary was prescribed to be 7.5 × 10^{-5} m s^{-1} corresponding to the lattice velocity of 1.5 × 10^{-4} lattice unit in the present LBM simulations. This value of velocity corresponds to the capillary number Ca of 4.5 × 10^{-7}, which is larger than that in a typical PEMFC operation where Ca is of the order of 10^{-8}. However, the two-phase transport with such a small capillary number still falls into the capillary fingering regime, and the results obtained based on network models showed that water transport had little influence with respect to the value of capillary number in the capillary fingering regime [14,17]. Thus, a large amount of simulation time can be saved in present study, comparing with the simulation of an extremely slow water transport process in actual PEMFCs.

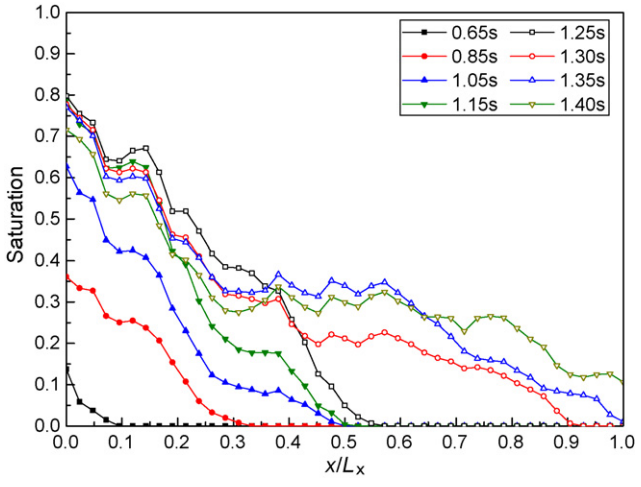

Fig. 6. Evolution of the water saturation profiles along the through-plane direction of the GDL with fiber contact angle of 145° and capillary number of 4.5 × 10^{-7}.

4.1. Water transport dynamics in the GDL with uniform wettability

Fig. 5(a) shows the simulated results of water transport process in the reconstructed GDL with a uniform fiber wettability of $\theta = 115°$. As shown, water invades into the GDL through the pores at the front surface of the GDL and forms convex water fronts due to the hydrophobic characteristic of the fibers. As more water invades and accumulates near the inlet of the GDL, liquid water selects some preferential paths to flow in the in-plane or through-plane direction of the GDL depending on the local capillary resistance force. This is very similar to the non-wetting phase invasion through a perforated plate in Fig. 3(a) that water (which is the non-wetting phase here) preferentially selects the largest pores encountered on its moving path. As water invades into the GDL further, some new water fronts are formed. Gradually, these water fronts combine into a main water front in the reconstructed GDL, and finally breakthrough the GDL (when the water front reaches the outlet of the GDL at $t = 1.45$ s) to form a droplet on the back surface of the GDL (at $t = 1.50$ s). The simulation results clearly described the water transport dynamics within the GDL and the formation of the droplet at preferential locations of the GDL surface, which is consistent with visualization experiments [6–8]. Sinha et al. [29] presented a similar water transport process by simulating water primary drainage in a more hydrophobic GDL (with $\theta = 140°$) using intermolecular potential two-phase LBM; however, the droplet formation was not considered in their study. Fig. 5(b) shows the corresponding variation of pressure difference between inlet and outlet with time during the water invasion process in the GDL. It can be seen that the pressure undergoes irregular oscillation during the invasion process, which implies the continuous buildup and release of the inlet pressure before and after the water front passing through the pores formed by fine fibers in the GDL to keep a constant water flux [9]. After the water breakthrough the GDL at $t = 1.45$ s, the pressure drops drastically and finally reaches a stable value when a steady droplet is formed. The breakthrough pressure at $t = 1.45$ s obtained from Fig. 5(b) is about 5.5 kPa, which is close to the experimental results for carbon paper [38] at 5.3–7.4 kPa.

Fig. 5(c) shows the cross-section images of water distribution along the GDL thickness at four different times. Comparing water distribution at $t = 0.85$ s and $t = 1.05$ s, it can be seen that water invasion in the GDL is not only along the through-plane direction and but also along the in-plane direction, as the pore space occupied by water in a certain cross-section gradually increases as the water front moves ahead. In addition, comparing water distribution at $t = 1.35$ s and $t = 1.50$ s, it is found that once the in-plane invasion process in a certain cross-section is completed, the void area which is available for gas transport remains and will have lit-

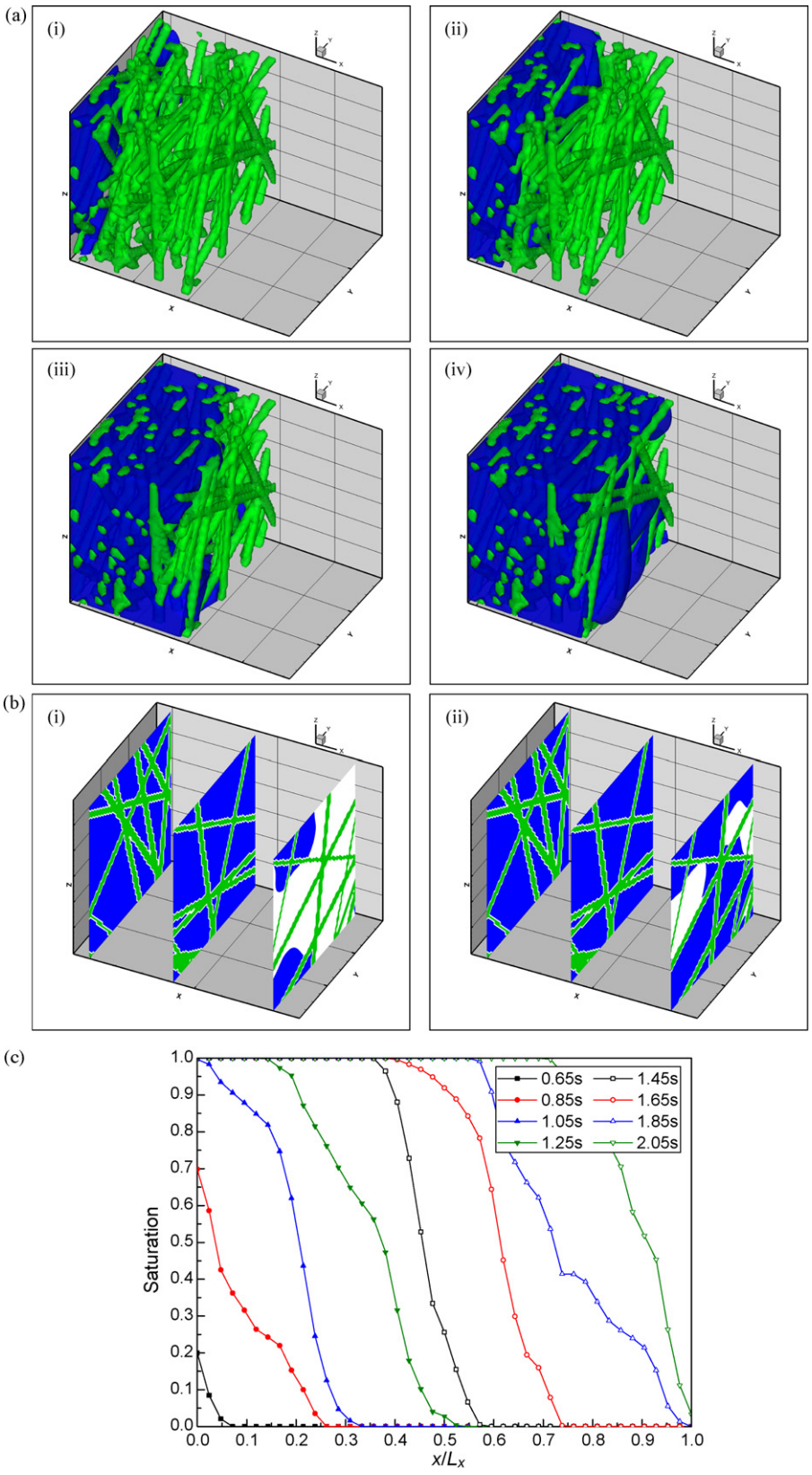

Fig. 7. (a) Snapshots of the water behavior in the reconstructed GDL microstructure with fiber contact angle of 92° and capillary number of 4.5×10^{-7} (blue area denotes the water). (i) $t = 0.85$ s, (ii) $t = 1.25$ s, (iii) $t = 1.85$ s, (iv) $t = 2.20$ s. (b) Cross-section images of water distribution in the reconstructed GDL with fiber contact angle of 92° and capillary number of 4.5×10^{-7} (blue area denotes the water). (i) $t = 1.85$ s, (ii) $t = 2.20$ s. (c) Evolution of the water saturation profiles along the through-plane direction of the GDL with fiber contact angle of 92° and capillary number of 4.5×10^{-7}. (For interpretation of the references to color in this figure legend, the reader is referred to the web version of the article.)

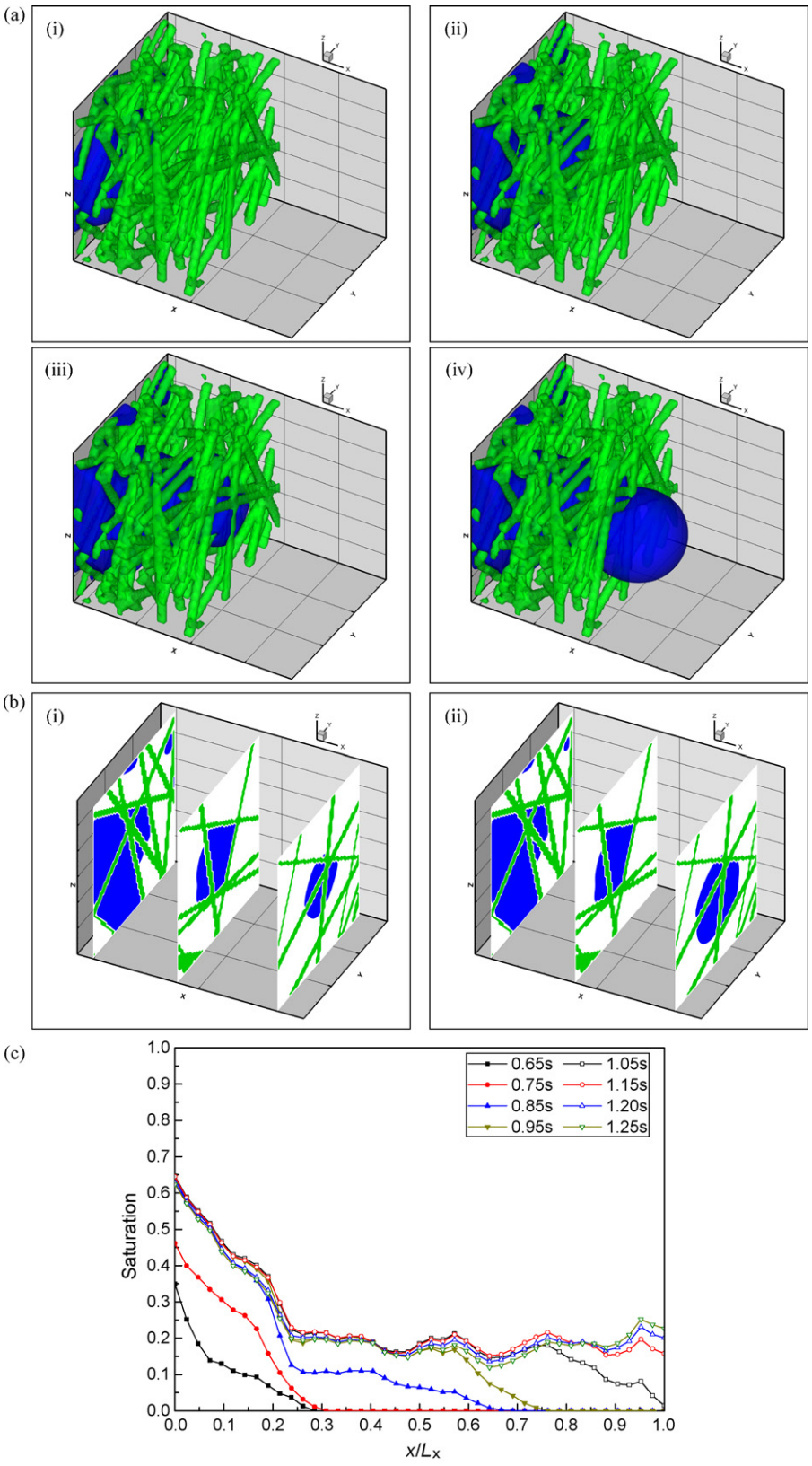

Fig. 8. (a) Snapshots of the water behavior in the reconstructed GDL microstructure with non-uniform wettability and capillary number of 4.5×10^{-7} (blue area denotes the water). (i) $t = 0.75$ s, (ii) $t = 0.95$ s, (iii) $t = 1.05$ s, (iv) $t = 1.20$ s. (b) Cross-section images of water distribution in the reconstructed GDL microstructure with non-uniform wettability and capillary number of 4.5×10^{-7} (blue area denotes the water). (i) $t = 1.05$ s, (ii) $t = 1.20$ s. (c) Evolution of the water saturation profiles along the through-plane direction of the GDL with non-uniform wettability and capillary number of 4.5×10^{-7}. (For interpretation of the references to color in this figure legend, the reader is referred to the web version of the article.)

tle change subsequently, though the water invasion in the though plane of the GDL has not finished. The evolution of the cross sectional average water saturation along the through-plane direction of the GDL is presented in Fig. 5(d). The cross sectional average saturation is defined as the ratio of the area occupied by water to the total pore area in the cross-section. It can be seen that the saturation profiles have complex but approximately concave shapes corresponding with capillary fingering invasion with small capillary number, which had been obtained by network simulations [14–17]. However, in contrast with the conclusion obtained by Lee et al. [16] in their network modeling that the saturation level in the GDL continues to increase after the breakthrough of water, the saturation profile in the GDL shown in Fig. 5(d) seems to have little change after the water breaks through the GDL at $t = 1.45$ s. It is also shown that the cross sectional average saturation near the front surface of the GDL reaches a stable value first, which is consistent with the evolution of the cross-section images of water distribution in Fig. 5(c). Also, it is shown that the average saturation is about 0.9 (and never reaches 1.0) at the inlet of GDL ($x/L_x = 0$) when the droplet forms, indicating that 10% of void space at the inlet is available for gas transport for the case with $\theta = 115^\circ$.

Water transport in the more hydrophobic GDL with a uniform fiber wettability of $\theta = 145^\circ$ was also investigated, and a similar water transport dynamic behavior to that of $\theta = 115^\circ$ was observed. Fig. 6 shows the corresponding saturation evolution profiles where the breakthrough time is identified as at $t = 1.35$ s. Thus, the breakthrough time decreases from 1.45 s to 1.35 s as the contact angle increases from 115° to 145°. Comparing Fig. 5(d) with Fig. 6, it can be seen that the saturation distribution curves for $\theta = 145^\circ$ have more obvious concave shapes than that for $\theta = 115^\circ$ and the water saturation in the cross-section is shown less in the GDL with more hydrophobicity. It also can be seen that the maximal average saturation at the inlet of the GDL is about 0.8 for the case of $\theta = 145^\circ$, indicating that 20% of void space is available for gas transport there, which is larger than 10% for the case of $\theta = 115^\circ$. All of the above indicate that the wettability of GDL indeed affects the water distribution in the GDL, and the enhancement of hydrophobicity of GDL is useful to provide more available pores or paths for gas transport through the GDL to catalyst layer. Again, this is contradictory to the results of a previous network model [16] indicating that hydrophobicity of GDL has no effect on water saturation distribution. In addition, it is observed from Fig. 6 that the cross sectional averaged saturations near the inlet of GDL are reduced after the breakthrough of water (at $t = 1.35$ s). This result further confirms the speculation of the capillary fingering transport mechanism in water invasion in GDL, which was proposed by Lister et al. [9] from their visualization study. As they have speculated, the dead ends are formed during the water invasion dominated by capillary fingering and these dead ends will recede from the GDL due to the inlet pressure drop if a breakthrough path adjacent to these dead ends is formed. The process described above is very similar to non-wetting phase invasion through a plate with openings of different sizes shown in Fig. 3(a) and (b). However, owing to the small cross sectional area of the GDL that was chosen in this study, the dead end receding and the resulting saturation reduction are not obvious for the case of $\theta = 115^\circ$ as shown in Fig. 5(d).

Figs. 7(a)–(c) shows that water transport in the GDL with almost neutral wettability of $\theta = 92^\circ$ exhibiting nearly stable displacement characteristics with rather flat and convex saturation profiles. It should be noted that the capillary number in Figs. 7(a)–(c) is the same as those for the cases of $\theta = 115^\circ$ and 145°, indicating that the flow is still dominated by capillary force. Again, it implies that the wettability also has significant influence on the two-phase flow in GDL. Actually, the phase diagram proposed by Lenormand [30] was based on their experiment with complete hydrophobicity ($\theta = 180^\circ$) of the non-wetting phase, where the wettability was not considered. From Eq. (19), it further predicts that the capillary resistance force for water invasion in the GDL will depends little on the pore size if the contact angel θ is close to 90°, thus resulting in the homogeneous invasion of the pores as the water front advances. Fig. 7(c) shows that the averaged saturation at inlet of the GDL reaches 1.0 after 1.05 s, indicating that the flooding occurs after 1.05 s for $\theta = 92^\circ$.

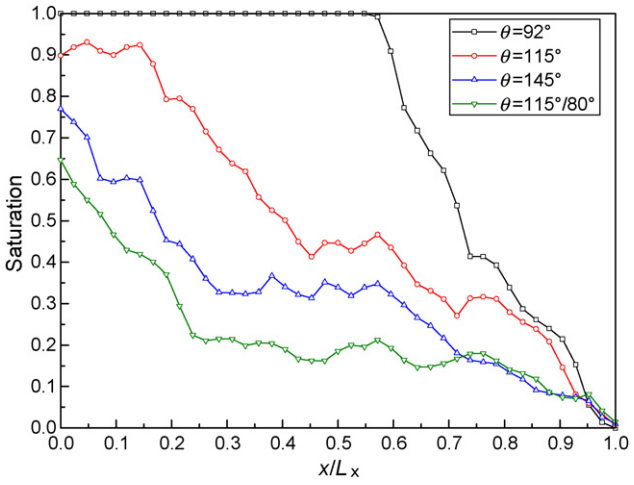

Fig. 9. Comparison of water saturation distribution along the through-plane direction of the GDL for non-uniform and uniform wettabilities at the time that water breakthrough occurs.

4.2. Water transport dynamics in the GDL with non-uniform wettability

In practice, the hydrophobicity of the GDL is achieved by treating the GDL with PTFE. However, due to the possible non-uniform loading of PTFE, hydrophobic and hydrophilic fractions generally coexist in the GDL. We now consider the GDL with non-uniform wettability in the present LBM study by prescribing a hydrophilic columnar subdivision along the thickness of the GDL, which is located in the middle of the reconstructed GDL with its diameter of 20 lattices. The contact angle of fibers in the hydrophilic subdivision was set to be 80° corresponding with the contact angle of carbon, while the rest was set to be 115° corresponding with the contact angle of pure PTFE material. Figs. 8(a) and (b) shows water transport behavior and Fig. 8(c) shows water saturation distribution evolution in the reconstructed GDL with prescribed coexisted wettabilities. It can be seen that water invades into the GDL selectively through the hydrophilic path while keeping other paths free for gas transport and the location of the water breakthrough occurred at the end of the hydrophilic path. The existence of hydrophilic path suppresses the formation of dead ends in the GDL, thus lowering the saturation near the inlet of the GDL. It is interesting to note from Fig. 8(c) that (i) the saturation at the inlet of GDL is 0.64 meaning that 36% of pore space at the inlet of GDL is available for gas transport, and (ii) the water saturation distribution in GDL has an almost flat variation with a value around 0.2 from $x/L_x = 0.25$ to the outlet after water breakthrough, which is different from the gradual decrease for uniform wettability cases shown in Figs. 5(d) and 6.

Fig. 9 shows the comparison of water saturation profiles along the thickness of the GDL at the time when water breakthrough occurs (for which the water front reaches the outlet of the GDL at $x/L_x = 1$) for non-uniform ($\theta = 115^\circ/80^\circ$) and uniform ($\theta = 92^\circ$, 115°, 145°) wettability distributions. It is shown that the reservation of a hydrophilic path in the GDL with non-uniform wettability of $\theta = 115^\circ/80^\circ$ reduces the saturation, even more obviously than enhancing hydrophobicity. Moreover, the average saturation in the

whole GDL with coexisting wettabilities is about 0.3 after water breaks through the GDL, while it is 0.4, 0.55 and 0.95 for uniform wetting GDL with 145°, 115° and 92° contact angles, respectively. This confirms the proposition by Sinha and Wang [15] that a GDL with tailored wettability distribution for both hydrophobic and hydrophilic paths is optimum for removal of liquid water from catalyst layer, thus alleviating mass transport losses in PEMFCs.

5. Concluding remarks

A profound understanding of liquid water transport in GDL is needed for improving performance of PEMFCs for the purpose of avoiding water flooding. The pore-scale modeling is regarded as a very useful tool to study water transport within the GDL, which can incorporate the wettability property and the realistic porous microstructure of the GDL together. In the present work, the water transport dynamic behavior in a carbon paper GDL with detailed microstructure reconstructed by stochastic method is investigated using the multiphase free-energy LBM approach. The water invasion processes through the GDL with a uniform inlet velocity are presented by considering uniform and non-uniform wettabilities of the GDL fibers, respectively. For a homogeneously wetting GDL with high hydrophobicity, the present results confirm the conclusion of previous network studies [14–17] that water transport in GDL is governed by capillary fingering at low capillary numbers, where water invasion in through-plane or in-plane direction depends only on the local capillary resistance. However, for a GDL with nearly neutral wettability, water transport exhibits stable displacement characteristics even for a capillary force dominated flow, implying that wettability is also an important parameter controlling the two-phase flow in GDL. Moreover, it is found that water in the non-uniform wetting GDL transports through the hydrophilic path preferentially. The simulations also show the formation of water droplets on the GDL surface for high hydrophilicity and non-uniform wettability cases. It is shown that the water breakthrough the GDL at preferential locations which can be regarded as the path ends of water transport in the GDL corresponding to the smallest capillary resistance. The resulting water saturation distributions show little change after the breakthrough of water occurs, which is quite different from the results from network modeling [16] showing that the saturation continuously increases for a long time after the breakthrough. The results also show significant effects of wettability on the water saturation distribution in GDL. Comparing the cross-section water saturation distributions in uniform and non-uniform wetting GDL, it is shown that the design of proper hydrophilic passages in the GDL can reduce the cross sectional average saturation not only at the inlet face but also in the whole GDL, thus leaving more void space for reactant gas transport to the catalyst layer. As point out by Sinha and Wang [15], treatment of the GDL with controlled wettability is extremely challenging, and novel wet coating technology is needed to be developed in the future.

As indicated in previous discussion, it is difficult to perform experimental studies for quantitative investigations of water transport behavior and water saturation distribution in the very thin GDL now, due to the limitations of the existing experimental methods, which results in the lack of the verification for simulation studies. Thus, it is imperative to develop accurate and effective experimental techniques to obtain complete 3D images of water distribution in GDL. Until that time, the pore-scale simulations by LBM model can be regarded as a necessary complement to the experimental studies at the present time.

Acknowledgement

This work was supported by the National Natural Science Foundation of China through Grant No. 50536010 and by Nissan Company.

References

[1] C.Y. Wang, in: W. Lietsich, A. Lamm, H.A. Gasteiger (Eds.), Handbook of Fuel Cells: Fundamentals, Technology and Applications, vol. 3, part 3, John Wiley & Sons, Chichester, 2003.
[2] K. Tüber, D. Pócza, C. Hebling, J. Power Sources 124 (2003) 403–414.
[3] J.H. Nam, M. Kaviany, Int. J. Heat Mass Transfer 46 (2003) 4595–4611.
[4] U. Pasaogullari, C.Y. Wang, J. Electrochem. Soc. 152 (2005) A380–A390.
[5] Y. Wang, C.Y. Wang, J. Electrochem. Soc. 153 (2006) A1193–A1200.
[6] C. Ziegler, D. Gerteisen, J. Power Sources 188 (2009) 184–191.
[7] X.G. Yang, F.Y. Zhang, A.L. Lubawy, C.Y. Wang, Electrochem. Solid State Lett. 7 (2004) A408–A411.
[8] F.Y. Zhang, X.G. Yang, C.Y. Wang, J. Electrochem. Soc. 153 (2006) A225–A232.
[9] S. Litster, D. Sinton, N. Djilali, J. Power Sources 154 (2006) 95–105.
[10] P.K. Sinha, P. Halleck, C.Y. Wang, Electrochem. Solid State Lett. 9 (2006) A344–A348.
[11] N. Pekula, K. Heller, P.A. Chuang, A. Turhan, M.M. Mench, J.S. Brenizer, K. Ünlü, Nucl. Instrum. Methods Phys. Res. A 542 (2005) 134–141.
[12] M.A. Hickner, N.P. Siegel, K.S. Chen, D.S. Hussey, D.L. Jacobson, M. Arif, J. Electrochem. Soc. 155 (2008) B427–B434.
[13] C. Hartnig, I. Manke, R. Kuhn, N. Kardjilov, J. Banhart, W. Lehnert, Appl. Phys. Lett. 92 (2008) 134106.
[14] P.K. Sinha, C.Y. Wang, Electrochim. Acta 52 (2007) 7936–7945.
[15] P.K. Sinha, C.Y. Wang, Chem. Eng. Sci. 63 (2008) 1081–1091.
[16] K.J. Lee, J.H. Nam, C.J. Kim, Electrochim. Acta 54 (2009) 1166–1176.
[17] K.J. Lee, J.H. Nam, C.J. Kim, J. Power Sources 195 (2010) 130–141.
[18] V.P. Schulz, J. Becker, A. Wiegmann, P.P. Mukherjee, C.Y. Wang, J. Electrochem. Soc. 154 (2007) B419–B426.
[19] H.J. Vogel, J. Tölke, V.P. Schulz, M. Krafczyk, K. Roth, Vadose Zone J. 4 (2005) 380–388.
[20] C Pan, L.S. Luo, C.T. Miller, Comput. Fluids 35 (2006) 898–909.
[21] X. Shan, H. Chen, Phys. Rev. E 47 (1993) 1815–1819.
[22] M.R. Swift, E. Orlandini, W.R. Osborn, J.M. Yeomans, Phys. Rev. E 54 (1996) 5041–5052.
[23] P. Yuan, L. Schaefer, Phys. Fluids 18 (2006) 042101.
[24] C. Pan, M. Hilpert, C.T. Miller, Water Resour. Res. 40 (2004) W01501.
[25] J. Park, M. Matsubara, X. Li, J. Power Sources 173 (2007) 404–414.
[26] L. Hao, P. Cheng, J. Power Sources 186 (2008) 104–114.
[27] J. Park, X. Li, J. Power Sources 178 (2008) 248–257.
[28] X.D. Niu, T. Munekata, S.A. Hyodo, K. Suga, J. Power Sources 172 (2007) 542–552.
[29] P.K. Sinha, P.P. Mukherjee, C.Y. Wang, J. Mater. Chem. 17 (2007) 3089–3103.
[30] R. Lenormand, J. Phys.: Condens. Matter 2 (1990) SA79–SA88.
[31] R.P. Ewing, B. Berkowitz, Adv. Water Resour. 24 (2001) 309–323.
[32] M. Ferer, G.S. Bromhal, D.H. Smith, Physica A 311 (2002) 5–22.
[33] K. Schladitz, S. Peters, D. Reinel-Bitzer, A. Wiegmann, J. Ohser, Comput. Mater. Sci. 38 (2006) 56–66.
[34] X.Y. He, G.D. Doolen, J. Stat. Phys. 107 (2002) 309–327.
[35] L. Hao, P. Cheng, J. Power Sources 190 (2009) 435–446.
[36] G.G.M. van der Sman, S. van der Graaf, Comput. Phys. Commun. 178 (2008) 492–504.
[37] A.J. Briant, P. Papatzacos, J.M. Yeomans, Philos. Trans. R. Soc. Lond. A 360 (2002) 485–495.
[38] J. Benziger, J. Nehlsen, D. Blackwell, T. Brennan, J. Itescu, J. Membr. Sci. 261 (2005) 98–106.